Experimental study on low-altitude UAV-to-ground propagation characteristics in campus environment☆

Yuandi Zhang [a], Jiawangnan Lu [a], Hongtao Zhang [a], Ziyi Huang [a], César Briso-Rodríguez [b], Lei Zhang [a],*

[a] *College of Information Science and Technology, Donghua University, Shanghai 201620, China*
[b] *Department of Signal Theory and Communications, Universidad Politécnica de Madrid, 28031 Madrid, Spain*

ARTICLE INFO

ABSTRACT

In recent years, unmanned aerial vehicle (UAV)-to-ground wireless channels have become focused areas. Thus a better understanding of UAV-to-ground wireless channel characterizations is critical. The large-scale fading characterization is widely analyzed in many research works. Nevertheless, the small-scale fading characterization of low-altitude UAV-to-ground propagation has not been fully modeled. In this work, the close-in (CI) free space and floating-intercept (FI) path loss models are implemented to characterize large-scale fading. The large-scale parameters, i.e., path loss exponent (PLE), shadow fading standard deviation (STD), and shadow fading correlation coefficient, are carefully extracted, analyzed, and compared. Regarding small-scale fading, Akaike's Information Criteria (AIC) is used to find the most suitable fading distribution. In addition, fade depth (FD), level crossing rate (LCR), and average fade duration (AFD) are also calculated. The quantitative results and comparisons show a noticeable difference with ground propagation. The parameterized models are helpful for further understanding and deployment of UAV-to-ground wireless communication systems.

1. Introduction

Recently, unmanned aerial vehicle (UAV) has attracted attention in many industries, e.g., military, public, and civil applications [1]. In addition, the UAV is an essential aerial relay platform for broad coverage and high-speed data rates in wireless communication because of its low cost, small size, and high mobility [2]. For instance, in emergency communication scenarios, UAVs are often used as an alternative to traditional base stations (BSs), which act as access points (APs) to provide user equipments (UEs) with communication conditions [3]. Reliable knowledge of channel characterization is the foundation of the design and analysis of all wireless communication systems [4]. Thus, UAV-to-ground channel characterization analysis and modeling are critical in this context. Analysis of UAV-to-ground channel characteristics needs to consider many factors, such as frequency band, UAV altitude, and propagation scenarios, especially UAV altitude. The altitude of the UAV can vary widely due to its flexibility. It has been documented that the UAV's flight altitude can significantly impact signal propagation and change signal propagation conditions. For example, as UAV rises,

signal propagation conditions can change from non-line-of-sight (NLoS) to line-of-sight (LoS) [5].

In recent works, UAV-to-ground channel modeling was conducted for different scenarios. LoS and NLoS were simulated under an urban scenario with ray tracing in [6]. The large-scale fading is analyzed at 6–150 m through the close-in free space reference distance (CI) path loss model. The path loss exponent (PLE) and shadow fading standard deviation (STD) were derived that increase with altitude. However, the terrain features in the simulation only include buildings, which may deviate from the actual measurement results. Unlike ray tracing, measurements were conducted over cellular networks at UAV altitudes of 1.5 m, 15 m, 30 m, 60 m, and 120 m in [7]. The floating-intercept (FI) model fitted the path loss. As UAV altitude rose, the PLE and shadow fading STD decreased from 3.7 to 2.0 and 7.7 to 3.4 dB, respectively. The propagation environment is closer to free space as the UAV altitude increases. The high altitude (2.5 km/2.7 km) situation was analyzed in [8]. Same as [7], the UAV-to-ground channel has better communication quality in the case of 2.7 km. In summary, the altitude of the UAV is an essential factor affecting communication quality, and

---

* Corresponding author.

E-mail addresses: yuandi.zhang@mail.dhu.edu.cn (Y. Zhang), 2221964@mail.dhu.edu.cn (J. Lu), 1229125@mail.dhu.edu.cn (H. Zhang), 201100152@mail.dhu.edu.cn (Z. Huang), cesar.briso@upm.es (C. Briso-Rodríguez), lei.zhang@dhu.edu.cn (L. Zhang).

Fig. 1. Measurement environment.

choosing an appropriate path loss model is the key to understanding channel characterizations. Furthermore, most literature only models large-scale fading, such as [9,10].

The multipath effects cause small-scale fading; the existing study analyzes the small-scale fading relatively few. The time of arrival (ToA) of multipath components (MPCs) and the power of delay profiles (PDPs) were modeled in the open and suburban areas in [11]. In the suburban area, the ToA is larger, and PDPs are more uniform since the suburban area has many scatterers. The clusters are approximately equal in the open and suburban areas. Furthermore, the fade depth (FD), average fade duration (AFD), level crossing rate (LCR), and small-scale fading distribution for different frequency bands and UAV altitudes were modeled in [12]. It shows that the FD is independent of frequency. Moreover, the FD in NLoS is larger than that in LoS. At the largest frequency, the LCR and AFD reach the maximum and minimum, respectively. In addition, the distribution of small-scale fading is fitted by various distributions. The log–logistic distribution is the best-fitted distribution.

A few studies jointly investigate large-scale and small-scale fading for UAV-to-ground propagation. The composite channel modeling incorporating shadowing and multipath fading (small-scale fading) has been experimentally investigated in [13]. Two new shadowed double-scattering channel models are proposed. The double-Nakagami double inverse-gamma model is suitable for NLoS. The double-Nakagami single inverse-gamma is suitable for LoS. The authors also have suggested a novel method of selecting UAVs by utilizing the slow variations of the signal mean values for the UAV association. Finally, the rationality of the model and UAV selection strategy are verified by measured data.

This paper aims to comprehensively analyze UAV-to-ground channels' large-scale and small-scale fading under different UAV altitudes and environments. Our main contributions are summarized as follows.

- We extract large-scale fading at two UAV altitudes (35 m/70 m) in different environments at 3.5 GHz. The large-scale fading parameters were compared in various UAV-to-ground and other traffic scenarios.
- Existing works are unclear on small-scale fading. In this paper, Akaike's Information Criteria (AIC) is used to determine the best-fitted distribution of small-scale fading. The results show that the t Location–Scale distribution is the best-fitted distribution.
- Three fundamental parameters (FD, LCR, and AFD) are analyzed to study the complex behavior of small-scale fading in UAV-to-ground channels.

The remainder of this paper is organized as follows. In Section 2, we introduce the measurement campaign, including the measurement

Table 1
Sounder parameters.

Parameter	Value
Carrier frequency	3.5 GHz
Number of subcarriers	2301
Bandwidth	46 MHz
Number of TX antennas	1
TX antennas	Omnidirectional antenna
Transmit power	27 dBm
Number of RX antennas	128
RX antennas	Dual-polarized cylindrical array

system and measurement environment. Section 3 introduces the fundamentals of channel characterizations and details the extraction process of large-scale and small-scale fading parameters. Section 4 focuses on the analysis of parameters and compares them with relevant work to verify the rationality of the measurement results. Conclusions are drawn in Section 5.

2. Measurement campaign

2.1. Measurement system

The measurement system comprises the aerial transmitter (TX) on a UAV and the ground receiver (RX). TX payloads are carried by A "DJI Matrice 600 Pro" drone. The TX payload includes a portable battery for powering, a minicomputer creating baseband signal, a universal software radio peripheral (USRP) transmitting broadband signal (46 MHz), a global positioning system (GPS) to synchronize TX and RX, and an omnidirectional antenna. The RX is a cylindrical array. The cylinder comprises 16 linear arrays, each with four patch elements. Each patch element has two different ports (vertical polarization and horizontal polarization). Hence, the RX has $16 \times 4 \times 2 = 128$ antennas. This paper assumes that the aerial TX acts as an AP and the ground RX as a UE. The critical test system parameters were outlined in Table 1 [14]. Data were obtained from [15], whose data are available at [16].

2.2. Measurement environment

The measurement was taken at the University of Southern California (USC) Park Campus. Fig. 1 is an aerial view of the campus on Google Earth. There are four UEs on campus. UEs have been marked in Fig. 1. UE1 is placed in the parking lot. Except for the south, other directions are surrounded by buildings, so the probability of NLoS propagation is high. UE2 is far from buildings. The probability of LoS propagation is high. UE3 and UE4 are placed closer to compare the channel
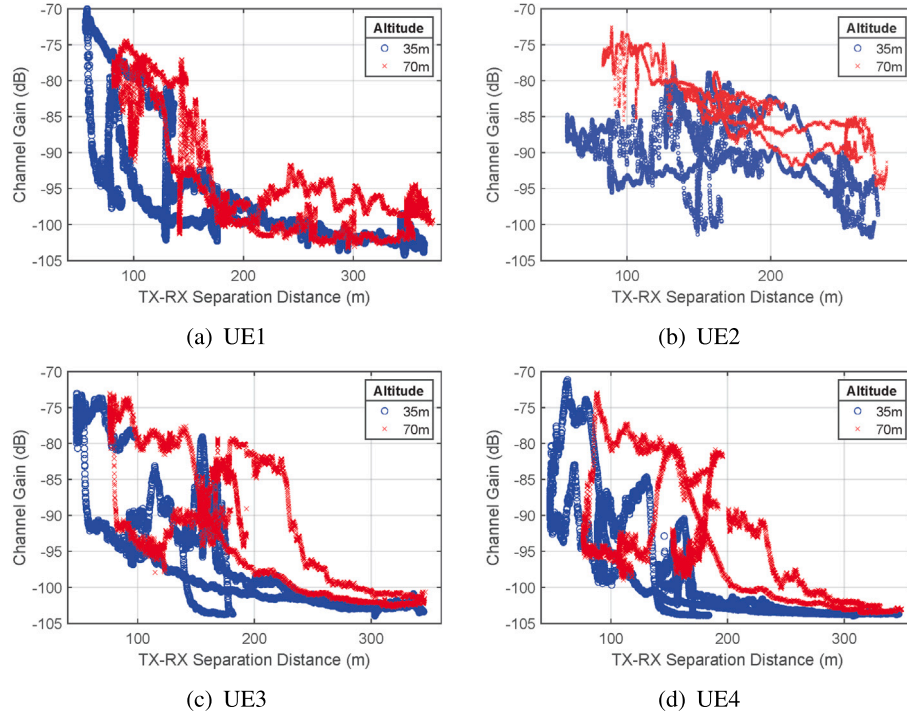
(a) UE1   (b) UE2

(c) UE3   (d) UE4

Fig. 2. Channel gain in all the measurement campaigns.

Table 2
Parameters used in the measurement.

Parameter		Value
Propagation environment		Campus
Measurement area		400 m × 200 m
Environment	UE1	dense
	UE2	sparse
	UE3	dense
	UE4	dense
Average UAV speed		4 m/s
UAV altitudes		35 m/70 m

characteristics difference between UE on the roadside and under the roof. However, the surrounding environment of the two is similar, and the probability of NLoS is also high. Compared with the four UEs, the environment of UE2 is more sparse, and other UEs are dense. The AP's flight trajectory is the same for different UEs. The solid white line in Fig. 1 is the AP's flight trajectory. The AP flies twice for each UE at different altitudes (35 m/70 m). To avoid noise interference, the measurement time was selected at dawn. The key environmental parameters are listed in Table 2 [15].

3. Result analysis and parameter extraction

3.1. Characterization of propagation channels

The design and analysis of any wireless communication system rely on accurate knowledge of the propagation channel. Fig. 3. shows the hierarchical relationships between channel characterizations. Channel characterizations include the large-scale fading and the small-scale fading.

For large-scale fading, the path loss is the attenuation in the transmitted signal while propagating from the TX to RX. Extensive terrain features such as trees, buildings, and dominant reflectors in specific cases cause shadow fading, which is the slow variation of received power. The large-scale fading is significant for communication systems

design at the network level. These effects can impact cellular coverage area and handoffs [4]. The path loss model estimates the power in received signals at varying TX-RX distances. Shadow fading distribution approximates the variability in received signal power near specific TX-RX separations [17]. Shadow fading autocorrelation is an essential characteristic besides distribution. It can provide a reference for AP location design and is defined as the correlation of shadow fading between different UEs and the same AP [18].

On the other hand, multipath propagation causes small-scale fading. The small-scale fading occurs when multiple signals between the TX and RX interfere, causing rapid variations in received power. Measuring bit error rates, AFDs, etc., is crucial for link-level performance [4]. Studying amplitude distribution can help to understand the random behavior of fading channels. FD and second-order statistics like the LCR, and AFD help analyze the severity of fading caused by spatial–temporal variations [19].

3.2. Channel gain for each UE

The channel gain describes the quality of the communication and determines other parameters, e.g., the PLE, the shadow fading STD, and the shadow fading autocorrelation coefficient.

This system obtains channel frequency response (CFR) through back-to-back (B2B) calibration [14]. The channel gain can be obtained by CFR. The channel gain is calculated as

$$G_{m,n}[\text{ dB}] = 10\log_{10}\left(\frac{\sum_{i=1}^{F} |H_{m,n,i}|^2}{F}\right), \tag{1}$$

where $H_{m,n,i}$ is the CFR between AP m and UE n at realization i. Each point frequency point in the measurement was viewed as a realization. $F = 2301$ is the number of subcarriers, and $G_{m,n}[\text{ dB}]$ is the sum of channel gain between AP m and UE n averaged over all realizations expressed in dB scale. Fig. 2 shows the channel gain in all the measurement campaigns. By analyzing the results, some preliminary observations can be drawn. Compared with the 35 m measurement, the 70 m measurement generally has higher channel gain. Because the occlusion of the buildings decreases in high altitudes, increasing
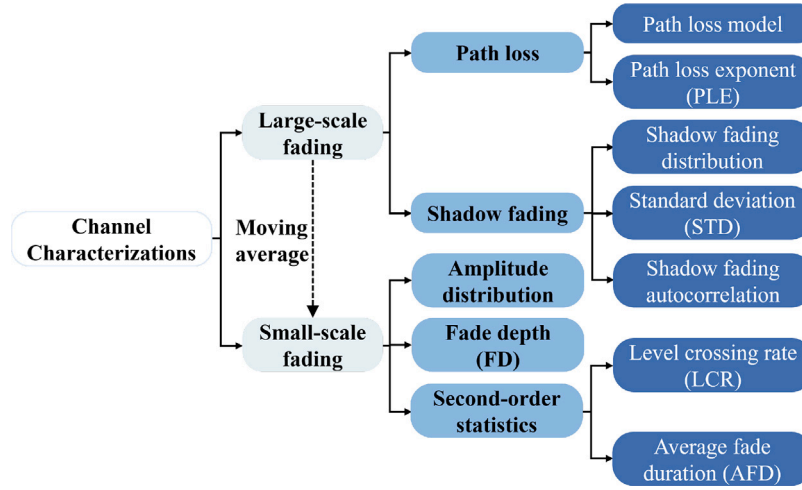
Fig. 3. Channel characterizations.

the probability of LoS propagation. UE2, away from buildings, has LoS paths in many areas, so it has higher channel gain than other UEs.

3.3. Path loss

Path loss can be computed by $PL[\text{dB}] = -10\log_{10}\left(\frac{\sum_{i=1}^{F}|H_{m,n,i}|^2}{F}\right)$ [20]. To remove the effects of small-scale fading, we perform a moving average of the path loss with a sliding window of 40 wavelengths [21]. The CI and FI path loss models are used to fit the path loss.

3.3.1. CI path loss model

The CI model is the widely used path loss model. The CI model can be calculated as

$$PL^{CI}(f,d)[\text{dB}] = PL_{FSPL}(d_0) + 10n\log_{10}\left(\frac{d}{d_0}\right) + X_\sigma^{CI}, \qquad (2)$$

where d is the separation distance between the TX and the RX, $PL^{CI}(f,d)[\text{dB}]$ represents the path loss with distance d at the measurement frequency f, $PL_{FSPL}(d_0)$ represents the free space path loss (FSPL) at the reference distance d_0, n is the PLE, X_σ^{CI} represents the shadow fading with standard deviation σ dB [22]. The CI model selects a distance d_0 based on physical propagation. In this paper, d_0 is 1 m. After calculating $PL_{FSPL}(d_0)$ based on d_0, we can use the minimum mean square error (MMSE) criterion to find n.

3.3.2. FI path loss model

The WINNER II and 3GPP standards have been widely used with the FI path loss model [23]. The FI path loss model is as follows

$$PL^{FI}(f,d)[\text{dB}] = \alpha + \beta\log_{10}(d) + X_\sigma^{FI}, \qquad (3)$$

where the parameter α is the intercept, β includes the PLE, X_σ^{FI} represents the shadow fading with STD σ dB. α and β can be obtained by the least squares (LS) method. The difference between the CI and FI models is that CI only has one parameter, the PLE. Fig. 4 gives an example of the path loss fitting at UE2 with an AP altitude of 70 m.

3.4. Distribution of shadow fading

The above formula can obtain the shadow fading values using simple subtraction. Shadow fading (in dB) is generally described as a normal distribution with zero mean $X \sim N[0,\sigma]$, where X is the shadow fading and $N[0,\sigma]$ denotes a normal distribution with zero mean, and an STD of σ [24]. Fig. 5 shows the fitting result of the shadow fading cumulative distribution function (CDF) at UE2 with an AP altitude of 70 m.
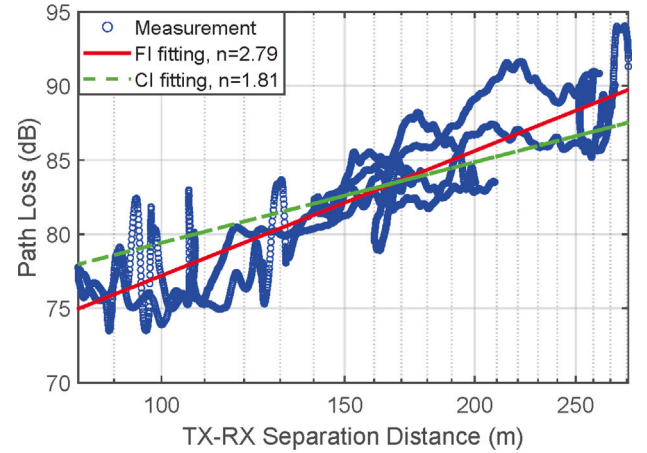

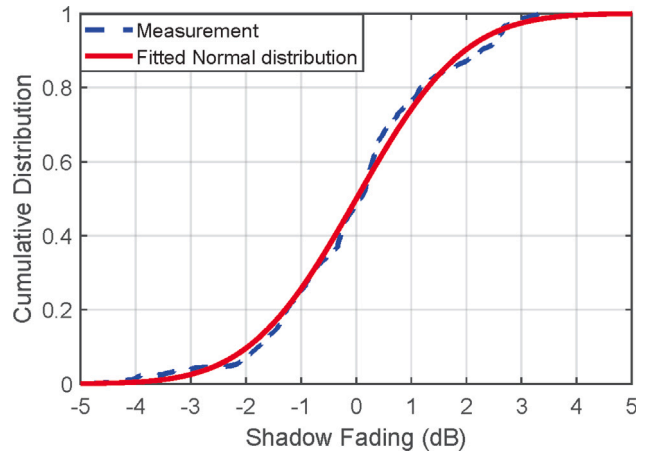Fig. 4. Path loss fitting at UE2 with an AP altitude of 70 m.

Fig. 5. Cumulative distribution of shadow fading at UE2 with an AP altitude of 70 m.
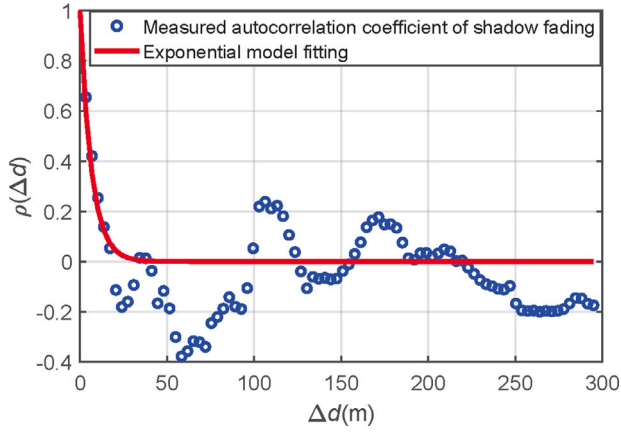
4

Fig. 6. Exponential model fitting of shadow fading autocorrelation coefficient at UE3 with an AP altitude of 35 m.
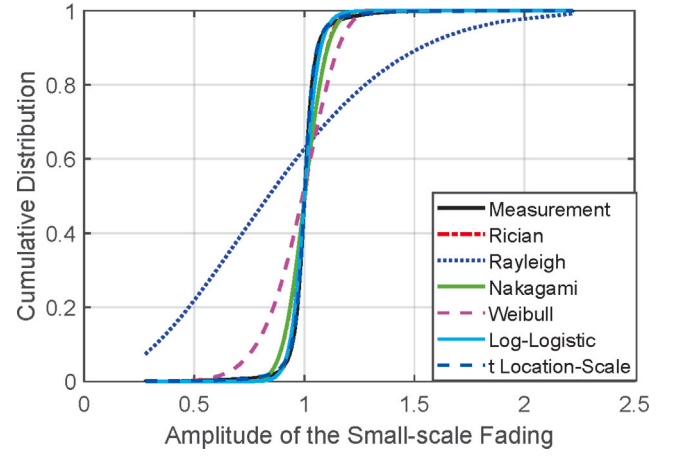

Fig. 7. CDF fitting of the small-scale fading at UE2 with an AP altitude of 70 m.

$$\rho\left(\Delta d\right) = \frac{\sum_{i=1}^{N}\left(X\left(d_i\right) - \overline{X\left(d\right)}\right) \cdot \left(X\left(d_i + \Delta d\right) - \overline{X\left(d + \Delta d\right)}\right)}{\sqrt{\sum_{i=1}^{N}\left(X\left(d_i\right) - \overline{X\left(d\right)}\right)^2} \cdot \sqrt{\sum_{i=1}^{N}\left(X\left(d_i + \Delta d\right) - \overline{X\left(d + \Delta d\right)}\right)^2}},$$

(4)

3.5. Shadow fading autocorrelation

The autocorrelation coefficient is often used to analyze the autocorrelation characterizations [18,25]. The definition is as shown in (4), where N is the number of samples, $X(d_i)$ denotes the shadow fading of the ith sample, $\overline{(\cdot)}$ is the sample mean, and $\overline{X(d)}$ denotes the shadow fading mean of samples. In (4), $\Delta d = k \cdot 40\lambda$, $k \in \mathbb{N}$ represents the distance difference between the AP and UE, where λ is the wavelength. $X\left(d_i + \Delta d\right)$ denotes the shadow fading at a distance Δd greater than the ith sample, and $\overline{X(d + \Delta d)}$ is the mean of $X\left(d_i + \Delta d\right)$.

An exponential model generally describes the shadow fading autocorrelation coefficient [26], which is expressed as $\rho\left(\Delta d\right) = \exp\left(-\frac{\Delta d}{d_{cor}}\right)$, where d_{cor} denotes the decorrelation distance, it depends on the scenario and is defined as the distance when $\rho\left(\Delta d\right)$ drops to $1/e$. Fig. 6 shows the shadow fading autocorrelation coefficient and the exponential model fitted by the least squares (LS) method at UE3 with an AP altitude of 35 m.

3.6. Small-scale fading distribution

The small-scale fading can be obtained by subtracting the moving average path loss from the raw path loss. In most cases, the Rayleigh and Rician distributions have been shown to describe the small-scale fading well. The Rayleigh distribution is often used to model NLoS channel, and the Rician distribution is often used to model LoS channel. Sometimes other distributions also are alternative solutions, such as the Nakagami, Weibull, Log–Logistic [12], and t Location–Scale distributions [27]. We used the Distribution Fitter tool in MATLAB to find the parameters that offer the best fit for different distributions. Fig. 7 shows the CDF fittings of the six distributions in the case of UE2 with an AP altitude of 70 m. The Rayleigh distribution fits worse than other distributions, meaning the UAV-to-ground channel does not fade as severely as the NLoS channel.

Akaike's Information Criteria (AIC) is introduced in [28] to find the best-fitted model for small-scale fading. AIC is a standard to measure the goodness of fit for a statistical model. It is calculated as $AIC =$ $-2log\left(\mathcal{L}\right) + 2K$, where $log(\cdot)$ is the natural logarithm, $\mathcal{L}$ is the likelihood function of the fitted model, and K is the number of free parameters in the model [29]. The model with the lowest AIC provides the best fit. The AIC value depends on the sample size. However, a single AIC is not interpretable. The AIC differences are defined for the convenience of comparison as $\Delta AIC_j = AIC_j - \min_i\left(AIC_i\right)$, where $\min_i\left(AIC_i\right)$ is the minimum AIC over $i=1, \ldots, J$ distribution models. So the ΔAIC value of the best-fitted model is 0. Then use the Akaike weight w_j to measure the fitting effect of different candidate models. w_j is defined as [30]

$$w_j = \frac{\exp\left(-\frac{1}{2}\Delta AIC_j\right)}{\sum_{i=1}^{J}\exp\left(-\frac{1}{2}\Delta AIC_i\right)},$$

(5)

where $\sum_{i=1}^{J} w_j = 1$. The one with the highest Akaike weight w_j is the best-fitted distribution.

3.7. Fade depth and second-order statistics

FD is defined by the difference in the small-scale fading between the 50% and 1% level values [31]. The LCR and AFD are collectively referred to as second-order statistics [32]. They are two critical statistical characterizations of mobile communication. LCR and AFD can be obtained by the received signal strength variations or the amplitude of the time-variant frequency as a function of time or distance. In this paper, since the distance between AP and UE is constantly fluctuating and not proportional to time, LCR and AFD are modeled as a function of time. According to the definition in [33], the LCR is the number of times the received signal crosses a level threshold per second, and the AFD is the time that is spent below the threshold. Considering the range of the measured small-scale fading amplitudes, we set the threshold at −6-6 dB. The LCR and AFD are normalized for ease of observation.

4. Analysis of channel characterization parameters

This section presents parameters extracted based on the abovementioned measurements, quantitatively analyzing the channel characteristics.

4.1. Large-scale fading

Table 3 presents the large-scale fading parameters for each case.

Table 3

Comparison of large-scale fading at different UEs and AP altitudes.

Location	AP altitude (m)	Path loss exponent (CI)	Path loss exponent (FI)	Shadow fading STD (dB)	Decorrelation distance (m)
UE1	35	2.34	3.03	3.92	10.02
	70	2.18	3.64	4.14	17.62
UE2	35	2.14	0.90	3.08	5.84
	70	1.81	2.86	1.54	4.30
UE3	35	2.36	2.75	3.37	6.54
	70	2.15	2.74	5.69	18.65
UE4	35	2.48	2.32	2.61	4.76
	70	2.27	1.91	4.37	14.04

4.1.1. Path loss exponent

Comparing the CI and FI models, the FI model is determined by the slope β and the intercept α, which depend on the measurement sample size and the corresponding distance. It has an excellent fitting on the distance within the measurement range. However, the FI model tends to make big errors when predicting the path loss at a longer distance that is not within the measurement range. The CI model has only one parameter, the PLE, but it refers to the free space path loss at 1 m, so it can stably fit measurement data of various scenarios and frequencies [34,35].

Table 3 shows that the PLE of the CI model is from 1.81 to 2.48, while the FI is from 0.90 to 3.64. The CI model can be used as a global standard to compare the path loss across frequencies and scenarios [36]. Therefore, we also use the CI model to analyze the PLE and shadow fading STD.

The PLEs are observed to be larger than 2 (free space PLE) except at UE2 70 m. This is because there are much more scatterers than free space. The LoS propagation probability is smaller. Also, diffraction is affected as the elevation angle is very low. At UE2 70 m, because UE2 is relatively sparse and the altitude of the AP is high, the LoS propagation probability is high. At the same time, due to reflection caused by scatterers, PLE is less than 2. From the perspective of all UE locations, UE2 has a smaller PLE. It is consistent with the higher channel gain at UE2 because higher channel gain causes lower path loss. Comparing different AP altitudes, the PLE of 70 m is smaller than that of 35 m, which implies that when the AP altitude is higher, the interference of the surrounding environment is less, and there is better communication quality. The same conclusion can be found in [7,8], and [37].

4.1.2. Shadow fading STD

The shadow fading STD fitted to the normal distribution ranged from 1.54 to 5.69 dB. Shadow fading STD at UE2 is still minimal compared to other UEs. Because shadow fading is caused by scatterers such as buildings and trees. UE2 has a more open environment and fewer scatterers than other UEs. When the altitude increases, the shadow fading STD of UE2 decreases, while that of UE1, UE3, and UE4 increases. This change may depend on the surrounding environment. In [38], it pointed out that the STD of shadow fading did not change much with the AP altitude change. Because its environment is rural and the buildings are sparse. Whereas in [7], the shadow fading STD decreases with altitude, just like UE2 of this work. It is speculated that few buildings can block the signal propagation at high altitude, and the LoS propagation probability further increase. Whether it is a sparse or dense area, the shadow fading STD is smaller than that of 3GPP, where shadow fading is suggested as 4 dB and 6 dB for the LoS and NLoS, respectively [12].

4.1.3. Autocorrelation characteristics of shadow fading

The values of decorrelation distances are 4.76–10.02 m and 4.3–18.65 m at AP altitudes of 35 m and 70 m, respectively. Consistent with

the shadow fading STD, the decorrelation distance increases with the AP altitude except for UE2. It implies the decorrelation of received signals at lower AP altitudes is favorable. The decorrelation distance of the UAV-to-ground channel is much smaller than those of other scenarios. In the urban macro scenario, the decorrelation distance reaches 32 m to 97 m [39]. In different high-speed railway scenarios, such as viaduct and cutting, they are 115.44 m and 88.78 m, respectively. However, in the curved tunnel, the decorrelation distance (1.86–16.75 m) is smaller than that in this work [18]. The shadow fading component in the UAV-to-ground scenario varies faster than other open scenarios, and the design of UAV-to-ground communication systems requires special attention.

4.1.4. Integration and comparison of the large-scale fading of the UAV-to-ground scenarios

The large-scale fading in various UAV-to-ground scenarios is summarized in Table 4. Since decorrelation distance is unavailable in most literature, only PLE and shadow fading STD are compared in this section. The PLEs in the other paper are around 2. The PLEs of this paper are also 1.81–2.48. It shows that the results of this measurement are reasonable and valid. Nevertheless, the PLEs of [6,40] increase with the altitude of the UAV. [6] explained that as the UAV altitude increases, the range of the distances from the ground locations becomes smaller. The shadow fading STDs are roughly 2–6 dB. This paper is in the range of 1.54–5.69 dB. However, the shadow fading is fitted with the generalized Gamma distribution when the UAV altitude is 2.5 km in [8]. Comparing different frequencies, STD increases with frequency [9,12]. Generally, this measurement's results and extracted parameters are relatively reasonable.

Table 4 helps give a comprehensive insight into the propagation characteristics of the UAV-to-ground channel and corresponding engineering suggestions. For instance, UAVs need to be deployed more densely at lower altitudes when used in UAV emergency communications.

4.1.5. Integration and comparison of the large-scale fading of different traffic scenarios

A complete table (Table 5) is made to provide the PLE and shadow fading STD of the vehicle-to-vehicle (V2V), tunnel, and High-speed railway (HSR) scenarios.

Table 5 could help establish a comprehensive understanding of the large-scale fading characterizations in the main traffic scenarios. For the PLE, the V2V scenario is close to 2, while the tunnel scenario is far smaller than 2. Because the V2V scenario is often a LoS environment under the urban or suburban. There is no occlusion from buildings and trees in the V2V scenario. In the straight tunnel scenario, the PLE is often less than 2 due to the waveguide effect. But in the curved tunnel scenario, the PLE is larger than 2 [51]. In the high-speed railway (HSR) scenario, statistical models such as Extended Hata are used to fit, and there is no PLE. For the shadow fading STD, the tunnel scenario is more stable than other scenarios (between 4 and 5 dB), which is caused by the relatively stable environment of the tunnel. The environment of other scenarios is changeable, and the range of shadow fading STD fluctuates.

4.2. Small-scale fading

4.2.1. Akaike weight of different distributions

Table 6 lists the Akaike weights of different distribution models. The results clearly show that the t Location–Scale is the best-fitted distribution with the largest Akaike weight, and the Rayleigh has the lowest Akaike weight, indicating that Rayleigh is unsuitable for the UAV-to-ground scenario. The PDF of the t Location–Scale distribution

Table 4
Large-scale fading comparison of different UAV-to-ground channels.

Reference	Frequency	UAV altitude	Scenario	Path loss exponent	Shadow fading STD (dB)
	3.5 GHz	35 m 70 m	LoS/NLoS	2.14–2.48 1.81–2.27	2.61–3.92 1.54–5.69
[6]	×	6–150 m	LoS NLoS	2.00–2.60 5.60–8.80	1.20–1.65 6.52–8.39
[7]	800 MHz	1.5–120 m	×	2.00–3.70	3.40–7.70
[8]	900 MHz	2.5 km 2.7 km	Suburban	2.81 2.28	Gamma distribution 1.28
[9]	900 MHz 1.8 GHz 5 GHz	Ground-30 m	LoS Tree NLoS Brush NLoS	×	3.78–6.57 3.22–5.22 1.30–5.01
[10]	3.5–6.5 GHz	20 m	LoS NLoS	3.22–3.74 6.58	1.61–3.43 3.45
[11]	3.1–5.3 GHz	4–16 m	Open Suburban	2.54–2.94 2.61–3.03	2.80–4.02 4.31–5.30
[12]	1 GHz 4 GHz 12 GHz 24 GHz	Ground-24 m	LoS/NLoS	2.50–3.58 2.42–3.79 2.47–3.54 2.49–3.74	2.50–3.72 3.17–4.16 2.48–3.56 2.75–3.22
[40]	850 MHz	15–75 m	Suburban	2.02–2.71	5.90

Table 5
Large-scale fading comparison of various traffic scenarios.

Traffic scenario	Reference	Frequency	Path loss exponent	Shadow fading STD (dB)	Remark
UAV-to-ground		3.5 GHz	2.14–2.48 1.81–2.27	2.61–3.92 1.54–5.69	AP altitude: 35 m AP altitude: 70 m
Vehicle-to-vehicle (V2V)	[41]	5.9 GHz	1.83–1.92	4.96–6.07	Parking garages
	[42]	5.89 GHz	1.92	5.32	Urban
	[43]	5.9 GHz	1.48–1.55	2.63–3.67	with vehicle obstruction
	[44]	700 MHz 5.9 GHz	2.20–3.41	×	Rural, Urban, Highway
	[45]	5.9 GHz	1.66–2.53	3.36–5.94	Urban, Highway
	[46]	5.9 GHz	4.82–6.13	2.73–3.60	with soundproof walls Urban, Suburban
	[47]	6.75 GHz 30 GHz 30 GHz	1.99–2.73	1.16–2.73	Street canyon
Tunnel	[48]	2.8–5 GHz	0.57–0.82	2.7	Straight road
	[49]	954 MHz-2 GHz	1.40–2.03	4.36–4.95	Straight railway
	[50]	954 MHz-2 GHz	0.55–2.97	4.87–5.00	Curved railway
	[51]	2.4–5 GHz	5.49–7.13	2.75–4.17	Curved subway
High-speed railway (HSR)	[52]	930 MHz	2.36–0.43 h, $d \leq 400$ m 16.5–0.2 h, $d > 400$ m	2.00–2.32	Viaduct h: viaduct height d: distance
	[53]	930 MHz	Deep: $13.05e^{-0.039(w_u - w_l)}$ Low: $1.66w_l^2 - 58.51w_l + 517.6$	2.10–4.50	Cutting w_u: upper width w_l: lower width
	[54]	930 MHz	Hata	1.88–4.73	Crossing bridge Excess loss (dB): 5.96–14.18
	[55]	930 MHz	Hata	1.57–3.92	Train station Excess loss (dB): 0.37–21.80

Table 6
Akaike wight of different distribution candidates.

Location	Altitude (m)	Rician	Rayleigh	Nakagami	Weibull	Log–Logistic	**t Location–Scale**
UE1	35	0.0000	0.0000	0.0000	0.0000	0.0322	**0.9678**
	70	0.0009	0.0000	0.0013	0.0000	0.1377	**0.8602**
UE2	35	0.0233	0.0000	0.0323	0.0002	0.4685	**0.4757**
	70	0.0003	0.0000	0.0002	0.0000	0.0698	**0.9297**
UE3	35	0.0000	0.0000	0.0000	0.0000	0.0469	**0.9531**
	70	0.0336	0.0000	0.0348	0.0005	0.3284	**0.6027**
UE4	35	0.0000	0.0000	0.0000	0.0000	0.0006	**0.9994**
	70	0.0062	0.0000	0.0070	0.0000	0.2081	**0.7787**

Table 7
Fade depth for small-scale fading.

Location	AP altitude (m)	1% (dB)	50% (dB)	Fading depth (dB)
UE1	35	−1.5406	−0.0039	1.5366
	70	−1.6302	0.0000	1.6302
UE2	35	−1.6417	−0.0039	1.6378
	70	−1.0648	0.0056	1.0704
UE3	35	−1.1376	−0.0007	1.1369
	70	−0.9119	−0.0006	0.9113
UE4	35	−1.0386	−0.0017	1.0369
	70	−0.9360	0.0003	0.9363

Fig. 9. Normalized AFD at UE2 and UE4.

for the 35 m. Fig. 9 is the normalized AFD of each case. The AFD is proportional to the level threshold. The AFD curve at 70 m is above 35 m (threshold < 0 dB), indicating that UE experiences longer fading when AP at lower altitudes. Therefore, the UAV altitude needs extra attention when deploying the UAV-to-ground communication system.

5. Conclusion

This paper investigates the low-altitude UAV-to-ground channels in sparse and dense environments. The critical large-scale and small-scale channel parameters, including the PLE, shadow fading STD, decorrelation distance, the amplitude of small-scale fading, FD, LCR, and AFD, are comprehensively analyzed and modeled. The PLEs are 2.14–2.48 and 1.81–2.27 at 35 m and 70 m, so the UAVs (APs) can be deployed more sparsely at higher altitudes. Observing the PLEs of sparse areas (1.81–2.14) and dense areas (2.15–2.48), communication quality is better in sparse areas. The shadow fading STD and decorrelation distance of shadow fading in sparse areas are smaller, indicating that the fluctuation of shadow fading in the sparse area is smaller, and the correlation is lower than in the dense area. Viewed from different altitudes, the STDs and decorrelation distances in the sparse area decrease as the UAV altitude increases. In contrast, in dense areas, it increases. For the small-scale parameters, the t Location–Scale distribution is the best-fitted distribution. The FDs, LCRs, and AFDs are smaller when the UAV altitude is 70 m than 35 m, which shows that the UAV-to-ground channel has better communication quality in higher altitudes. This work's qualitative analysis and corresponding findings can be applied to design and optimize UAV-to-ground wireless communication systems.

In future work, we can use machine learning (ML) to channel modeling. For example, we can predict the parameters of the path loss model using Bayesian or Artificial Neural Network (ANN) methods [56]. We can classify clusters using the k-means algorithm and estimate the MPCs' ToA, angle of arrival (AoA), etc. [57].
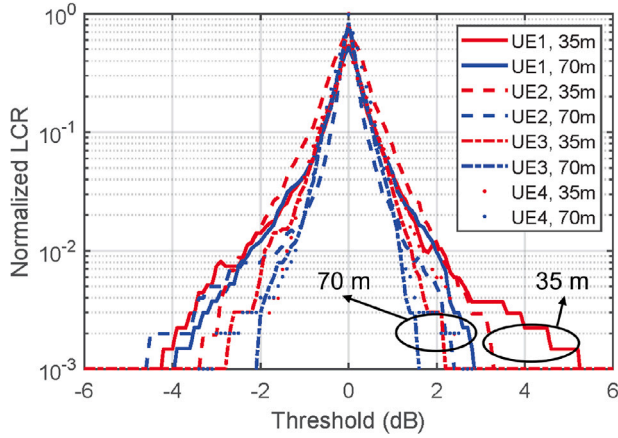

Fig. 8. Normalized LCR at UE2 and UE4.

is provided.

$$f(x) = \frac{\Gamma\left(\frac{\upsilon+1}{2}\right)}{\sigma\sqrt{\upsilon\pi}\,\Gamma\left(\frac{\upsilon}{2}\right)} \left[\frac{\upsilon + \left(\frac{x-\mu}{\sigma}\right)^2}{\upsilon}\right]^{-\left(\frac{\upsilon+1}{2}\right)}, \tag{6}$$

where $\Gamma(\cdot)$ is the gamma function, μ is the location parameter, σ is the scale parameter, and υ is the shape parameter [27]. The location parameter μ is close to 1 in different cases.

4.2.2. Fade depth and second-order statistics

Table 7 summarizes the FD. Except for UE1, the FD of low altitudes is larger, which implies that UAV-to-ground channels experience more severe fading at lower altitudes.

Fig. 8 is the normalized LCR of different cases. It shows that the LCR peaks when the level threshold is 0 dB, which means that the small-scale fading fluctuates the most around 0 dB. The LCR at 35 m is larger than that at 70 m, which illustrates that the fading is more variable
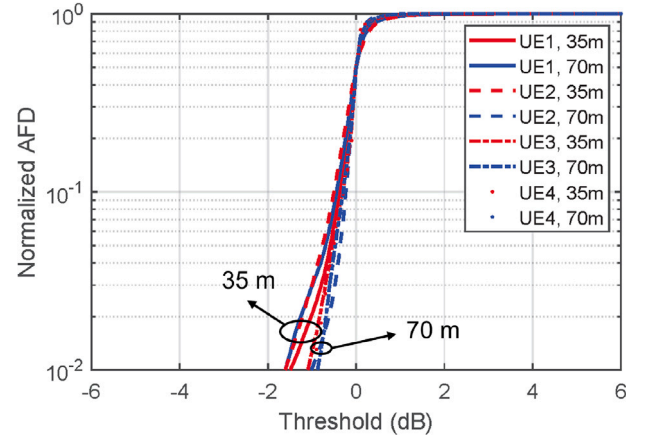
CRediT authorship contribution statement

Yuandi Zhang: Data curation, Formal analysis, Validation, Writing – original draft. **Jiawangnan Lu:** Investigation, Writing – original draft. **Hongtao Zhang:** Investigation, Data curation. **Ziyi Huang:** Investigation, Formal analysis. **César Briso-Rodríguez:** Supervision, Writing – review & editing. **Lei Zhang:** Conceptualization, Methodology, Supervision, Writing – review & editing.

Declaration of competing interest

The authors declare that they have no known competing financial interests or personal relationships that could have appeared to influence the work reported in this paper.

Data availability

Data will be made available on request.

References

[1] L. Gupta, R. Jain, G. Vaszkun, Survey of important issues in UAV communication networks, IEEE Commun. Surv. Tutor. 18 (2) (2015) 1123–1152.
[2] H. Kim, J. Ben-Othman, A collision-free surveillance system using smart UAVs in multi domain IoT, IEEE Commun. Lett. 22 (12) (2018) 2587–2590.
[3] S. Yin, L. Li, F.R. Yu, Resource allocation and basestation placement in downlink cellular networks assisted by multiple wireless powered UAVs, IEEE Trans. Veh. Technol. 69 (2) (2019) 2171–2184.
[4] X. Yin, X. Cheng, Characterization of propagation channels, in: Propagation Channel Characterization, Parameter Estimation, and Modeling for Wireless Communications, IEEE, 2016, pp. 15–40.
[5] Z. Cui, C. Briso-Rodriguez, K. Guan, C. Calvo-Ramírez, B. Ai, Z. Zhong, Measurement-based modeling and analysis of UAV air-ground channels at 1 and 4 GHz, IEEE Antennas Wirel. Propag. Lett. 18 (9) (2019) 1804–1808.
[6] G.E. Athanasiadou, G.V. Tsoulos, Path loss characteristics for UAV-to-ground wireless channels, in: 2019 13th European Conference on Antennas and Propagation, IEEE, EuCAP, 2019, pp. 1–4.
[7] R. Amorim, H. Nguyen, P. Mogensen, I.Z. Kovács, J. Wigard, T.B. Sørensen, Radio channel modeling for UAV communication over cellular networks, IEEE Wirel. Commun. Lett. 6 (4) (2017) 514–517.
[8] J. Liu, H. Zhang, M. Sheng, Y. Su, S. Chen, J. Li, High altitude air-to-ground channel modeling for fixed-wing UAV mounted aerial base stations, IEEE Wirel. Commun. Lett. 10 (2) (2020) 330–334.
[9] Y. Shi, R. Enami, J. Wensowitch, J. Camp, Measurement-based characterization of LOS and NLOS drone-to-ground channels, in: 2018 IEEE Wireless Communications and Networking Conference, WCNC, IEEE, 2018, pp. 1–6.
[10] Y. Lv, Y. Wang, J. Chai, W. Wang, Ultra wideband channel measurement and analysis for low altitude UAV air-to-ground scenario, in: 2021 13th International Symposium on Antennas, Propagation and EM Theory, ISAPE, IEEE, 2021, pp. 1–3.
[11] W. Khawaja, I. Guvenc, D. Matolak, UWB channel sounding and modeling for UAV air-to-ground propagation channels, in: 2016 IEEE Global Communications Conference, GLOBECOM, IEEE, 2016, pp. 1–7.
[12] Z. Cui, C. Briso-Rodriguez, K. Guan, Z. Zhong, F. Quitin, Multi-frequency air-to-ground channel measurements and analysis for UAV communication systems, IEEE Access 8 (2020) 110565-110574.
[13] P.S. Bithas, V. Nikolaidis, A.G. Kanatas, G.K. Karagiannidis, UAV-to-Ground communications: channel modeling and UAV selection, IEEE Trans. Commun. 68 (8) (2020) 5135–5144.
[14] J. Gomez-Ponce, T. Choi, N.A. Abbasi, A. Adame, A. Alvarado, C. Bullard, R. Shen, F. Daneshgaran, H.S. Dhillon, A.F. Molisch, Air-to-ground directional channel sounder with drone and 64-antenna dual-polarized cylindrical array, in: 2021 IEEE International Conference on Communications Workshops, ICC Workshops, IEEE, 2021, pp. 1–6.
[15] T. Choi, J. Gomez-Ponce, C. Bullard, I. Kanno, M. Ito, T. Ohseki, K. Yamazaki, A.F. Molisch, Using a drone sounder to measure channels for cell-free massive MIMO systems, in: 2022 IEEE Wireless Communications and Networking Conference, WCNC, IEEE, 2022, pp. 2506–2511.
[16] T. Choi, J. Gomez-Ponce, C. Bullard, I. Kanno, M. Ito, T. Ohseki, K. Yamazaki, A.F. Molisch, Open-Source Cell-Free Massive MIMO Channel Data 2020. URL: https://wides.usc.edu/research_matlab.html.
[17] S. Kurt, B. Tavli, Path-loss modeling for wireless sensor networks: a review of models and comparative evaluations, IEEE Antennas Propag. Mag. 59 (1) (2017) 18–37.
[18] K. Guan, B. Ai, Z. Zhong, C.F. López, L. Zhang, C. Briso-Rodriguez, A. Hrovat, B. Zhang, R. He, T. Tang, Measurements and analysis of large-scale fading characteristics in curved subway tunnels at 920 MHz, 2400 MHz, and 5705 MHz, IEEE Trans. Intell. Transp. Syst. 16 (5) (2015) 2393–2405.
[19] A.A. Khuwaja, Y. Chen, N. Zhao, M.-S. Alouini, P. Dobbins, A survey of channel modeling for UAV communications, IEEE Commun. Surv. Tutor. 20 (4) (2018) 2804–2821.
[20] B. Ai, et al., On indoor millimeter wave massive MIMO channels: measurement and simulation, IEEE J. Sel. Areas Commun. 35 (7) (2017) 1678–1690.
[21] W.C. Lee, Estimate of local average power of a mobile radio signal, IEEE Trans. Veh. Technol. 34 (1) (1985) 22–27.
[22] K. Mao, Q. Zhu, Y. Qiu, X. Liu, M. Song, W. Fan, A.B.J. Kokkeler, Y. Miao, A uav-aided real-time channel sounder for highly dynamic nonstationary A2G scenarios, IEEE Trans. Instrum. Meas. 72 (2023) 1–15.
[23] T.A. Thomas, M. Rybakowski, S. Sun, T.S. Rappaport, H. Nguyen, I.Z. Kovacs, I. Rodriguez, A prediction study of path loss models from 2-73.5 GHz in an urban-macro environment, in: 2016 IEEE 83rd Vehicular Technology Conference, VTC Spring, IEEE, 2016, pp. 1–5.
[24] B. Hua, H. Ni, Q. Zhu, C.-X. Wang, T. Zhou, K. Mao, J. Bao, X. Zhang, Channel modeling for uav-to-ground communications with posture variation and fuselage scattering effect, IEEE Trans. Commun. 71 (5) (2023) 3103–3116.
[25] M. Series, Guidelines for evaluation of radio interface technologies for IMT-Advanced, Rep. ITU 638 (2009) 1–72.
[26] F. Graziosi, F. Santucci, A general correlation model for shadow fading in mobile radio systems, IEEE Commun. Lett. 6 (3) (2002) 102–104.
[27] P. Tedeschi, S. Sciancalepore, R. Di Pietro, Modelling a communication channel under jamming: experimental model and applications, in: 2021 IEEE Intl Conf on Parallel & Distributed Processing with Applications, Big Data & Cloud Computing, Sustainable Computing & Communications, Social Computing & Networking, ISPA/BDCloud/SocialCom/SustainCom, New York City, NY, USA, 2021, pp. 1562–1573.
[28] L. Zhang, J. Rodríguez-Piñeiro, J.R. Fernández, J.A. García-Naya, D.W. Matolak, C. Briso, L. Castedo, Propagation modeling for outdoor-to-indoor and indoor-to-indoor wireless links in high-speed train, Measurement 110 (2017) 43–52.
[29] K.P. Burnham, D.R. Anderson, Multimodel inference: understanding AIC and BIC in model selection, Sociol. Methods Res. 33 (2) (2004) 261–304.
[30] R. He, Z. Zhong, B. Ai, J. Ding, Y. Yang, A.F. Molisch, Short-term fading behavior in high-speed railway cutting scenario: Measurements, analysis, and statistical models, IEEE Trans. Antennas and Propagation 61 (4) (2012) 2209–2222.
[31] S. Kozono, Received signal-level characteristics in a wide-band mobile radio channel, IEEE Trans. Veh. Technol. 43 (3) (1994) 480–486.
[32] M.C. Stefanovic, M.D. Petkovic, Envelope level crossing rate of cosine sinal ithi Nakagami-q interference, in: 2007 8th International Conference on Telecommunications in Modern Satellite, Cable and Broadcasting Services, IEEE, 2007, pp. 533–536.
[33] Multipath propagation and parameterization of its characteristics, document Rec. ITU-R P.1407-6, ITU-R, 2017.
[34] T.S. Rappaport, G.R. MacCartney, M.K. Samimi, S. Sun, Indoor office wideband millimeter-wave propagation measurements and channel models at 28 and 73 GHz for ultra-dense 5G wireless networks, IEEE Access 3 (2015) 2388–2424.
[35] S. Sun, T.S. Rappaport, T.A. Thomas, A. Ghosh, H.C. Nguyen, I.Z. Kovacs, I. Rodriguez, O. Koymen, A. Partyka, Investigation of prediction accuracy, sensitivity, and parameter stability of large-scale propagation path loss models for 5G wireless communications, IEEE Trans. Veh. Technol. 65 (5) (2016) 2843–2860.
[36] T.S. Rappaport, G.R. MacCartney, M.K. Samimi, S. Sun, Wideband millimeter-wave propagation measurements and channel models for future wireless communication system design, IEEE Trans. Commun. 63 (9) (2015) 3029–3056.
[37] X. Cai, J. Rodríguez-Piñeiro, X. Yin, N. Wang, B. Ai, G.F. Pedersen, A.P. Yuste, An empirical air-to-ground channel model based on passive measurements in LTE, IEEE Trans. Veh. Technol. 68 (2) (2018) 1140–1154.
[38] J. Lu, Y. Zhang, L. Zhang, Research on UAV-to-ground communication channel based on NYUSIM, in: 2022 IEEE 5th International Conference on Electronic Information and Communication Technology, ICEICT, IEEE, 2022, pp. 432–437.
[39] Y. Zhang, J. Zhang, D. Dong, X. Nie, G. Liu, P. Zhang, A novel spatial autocorrelation model of shadow fading in urban macro environments, in: IEEE GLOBECOM 2008-2008 IEEE Global Telecommunications Conference, IEEE, 2008, pp. 1–5.
[40] K. Tu, J. Rodríguez-Piñeiro, X. Yin, L. Tian, Low altitude air-to-ground channel modelling based on measurements in a suburban environment, in: 2019 11th International Conference on Wireless Communications and Signal Processing, WCSP, IEEE, 2019, pp. 1–6.
[41] M. Yang, B. Ai, R. He, L. Chen, X. Li, J. Li, Z. Zhong, V2V channel characterization and modeling for underground parking garages, China Commun. 16 (9) (2019) 93–105.
[42] J. Joo, O.S. Eyobu, D.S. Han, H.-J. Jeong, Measurement based V2V path loss analysis in urban NLOS scenarios, in: 2016 Eighth International Conference on Ubiquitous and Future Networks, ICUFN, IEEE, 2016, pp. 73–75.

[43] M. Yang, B. Ai, R. He, L. Chen, X. Li, Z. Huang, J. Li, C. Huang, Path loss analysis and modeling for vehicle-to-vehicle communications with vehicle obstructions, in: 2018 10th International Conference on Wireless Communications and Signal Processing, WCSP, IEEE, 2018, pp. 1–6.

[44] L. Rubio, V.M. Rodrigo-Peñarrocha, J. Reig, H. Fernández, Investigation of the path loss propagation for V2V communications in the opposite direction, in: 2016 IEEE International Symposium on Antennas and Propagation, APSURSI, IEEE, 2016, pp. 1685–1686.

[45] H. Fernández, V.M. Rodrigo-Penarrocha, L. Rubio, J. Reig, Path loss characterization in vehicular environments under LOS and NLOS conditions at 5.9 GHz, in: The 8th European Conference on Antennas and Propagation, EuCAP 2014, IEEE, 2014, pp. 3044–3048.

[46] C. Li, K. Yang, J. Yu, F. Li, Y. Shui, F. Chang, W. Chen, V2V radio channel performance based on measurements in ramp scenarios at 5.9 GHz, IEEE Access 6 (2018) 7503–7514.

[47] D. Dupleich, R. Müller, S. Skoblikov, C. Schneider, J. Luo, M. Boban, G. Del Galdo, R. Thomä, Multi-band characterization of path-loss, delay, and angular spread in V2V links, in: 2018 IEEE 29th Annual International Symposium on Personal, Indoor and Mobile Radio Communications, PIMRC, IEEE, 2018, pp. 85–90.

[48] J.-M. Molina-Garcia-Pardo, M. Lienard, P. Degauque, Propagation in tunnels, EURASIP J. Wireless Commun. Networking 2009 (2009) 1–9.

[49] N. Wang, A uniform path-loss model by power balance theory (PBT) and its application on tunnels, in: Proceedings of the 9th International Symposium on Antennas, Propagation and EM Theory, IEEE, 2010, pp. 481–484.

[50] Ningde High-Speed Railway Tunnel Covering Research Report, Tech. Rep., GCI Science & Technology Co. Ltd., Guangzhou, China, 2008.

[51] K. Guan, Z. Zhong, J.I. Alonso, C. Briso-Rodríguez, Measurement of distributed antenna systems at 2.4 GHz in a realistic subway tunnel environment, IEEE Trans. Veh. Technol. 61 (2) (2011) 834–837.

[52] R. He, Z. Zhong, B. Ai, J. Ding, Measurements and analysis of short-term fading behavior for high-speed rail viaduct scenario, in: 2012 IEEE International Conference on Communications, ICC, IEEE, 2012, pp. 4563–4567.

[53] R. He, Z. Zhong, B. Ai, J. Ding, Propagation measurements and analysis for high-speed railway cutting scenario, Electron. Lett. 47 (21) (2011) 1167–1168.

[54] K. Guan, Z. Zhong, B. Ai, T. Kürner, Propagation measurements and modeling of crossing bridges on high-speed railway at 930 MHz, IEEE Trans. Veh. Technol. 63 (2) (2013) 502–517.

[55] K. Guan, Z. Zhong, B. Ai, T. Kürner, Propagation measurements and analysis for train stations of high-speed railway at 930 MHz, IEEE Trans. Veh. Technol. 63 (8) (2014) 3499–3516.

[56] S.M. Aldossari, K.-C. Chen, Machine learning for wireless communication channel modeling: An overview, Wirel. Pers. Commun. 106 (2019) 41–70.

[57] M. Mohri, R. Afshin, T. Ameet Talwalkar, Foundations of Machine Learning, MIT Press, 2018.

Jiawangnan Lu is currently working toward the Master degree in Information and Communication Engineering with the College of Information Science and Technology, Donghua University, Shanghai, China. Her research interests include cellular network localization and trajectory prediction.

Hongtao Zhang received the M.S. degree in electrical engineering in 2022 from Donghua University, Shanghai, China, where he is currently working toward the Ph.D. degree in intelligent sensing and machine vision. His research interests include reinforcement learning, energy scheduling in microgrids.

Ziyi Huang is currently working toward the Master degree in Information and Communication Engineering with the College of Information Science and Technology, Donghua University, Shanghai, China. Her research interests include channel sounding and channel modeling.
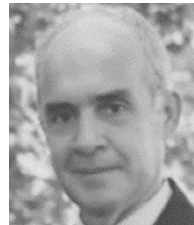
Cesar Briso was born in Valladolid, Spain, in 1968. He received the Ph.D. degree in mobile communications from the Universidad Politécnica de Madrid, Madrid, Spain, in 1998. In 2000, he became an Associate Professor with the Technical University of Madrid, Madrid, where he has been a Permanent Professor since 2008. He is currently an expert on the design of highfrequency systems for mission-critical communications and in propagation measurements and modeling in complex environments, such as tunnels, stations, and UAVs. He has made 30 industrial and research projects with national and international companies and institutions. He has authored 100 publications in international SCI journals and congress, and holds three patents. He was a recipient of the National Awards for the Best Ph.D. of the Spanish Association of Telecommunications Engineers.

Yuandi Zhang is currently working toward the Master degree in Information and Communication Engineering with the College of Information Science and Technology, Donghua University, Shanghai, China. His research interests include channel modeling and mobile edge computing.

Lei Zhang received the B.S. degree in communication engineering from Anhui University, Hefei, China, in 2009, and the M.S. and Ph.D. (Premio Extraordinario de Doctorado) degrees in telecommunications from the Universidad Politécnica de Madrid (UPM), Madrid, Spain, in 2013 and 2016, respectively. In 2016, he was a Visiting Scholar with the University of South Carolina, Columbia, SC, USA. From 2016 to 2017, he was a Research Assistant Professor with the Shanghai Institute of Microsystem and Information Technology, Chinese Academy of Science, Shanghai, China. Since 2019, he has been an Associate Professor with the College of Information Science and Technology, Donghua University, Shanghai. His research interests include wireless channel sounding & modeling, wearable computing.